

Measuring Topological Invariants and Protected Bound States in Disordered Discrete Time Quantum Walks

Sonja Barkhofen,¹ Thomas Nitsche,¹ Fabian Elster,¹ Lennart Lorz,¹ Aurél Gábris,^{2,3} Igor Jex,² and Christine Silberhorn¹

¹*Applied Physics, University of Paderborn, Warburger Strasse 100, 33098 Paderborn, Germany*

²*Department of Physics, Faculty of Nuclear Sciences and Physical Engineering,*

Czech Technical University in Prague, Břehová 7, 115 19 Praha 1-Staré Město, Czech Republic

³*Department of Theoretical Physics, University of Szeged, Tisza Lajos körút 84, H-6720 Szeged, Hungary*

(Dated: June 2, 2016)

The discovery of topological insulators sparked significant interest in the investigation of topological material properties. Quantum walks constitute a versatile platform for simulating transport phenomena including topological features in highly controllable setups. We experimentally implement the scheme proposed by Tarasinski et al. [Phys. Rev. A 89, 042327 (2014)] using our photonic time multiplexed discrete-time quantum walk system, directly accessing and measuring the relevant topological invariants. Our tunable coin operation allows to reach distinct topological phases, and accordingly observe topological phase transitions. Being able to read-out the position and the coin state, we measure scattered reflection amplitudes which are directly related to the topological invariants. By interfacing two samples with known, experimentally determined, topological invariants we observe localised edge states of verified topological origin. The predicted robustness of the found edge states against disorder and perturbation has been tested and verified in large ensemble measurements.

PACS numbers: 03.67.Ac, 42.50.-p, 03.65.Vf

Quantum walks [1–3] have gained recognition as a potential platform for quantum algorithms [4–8] and quantum simulators [9–13]. In the last years, they have been realized experimentally in various systems, demonstrating different effects known from condensed matter physics such as dynamical localization [14–16], percolation [17], interacting systems [18, 19], and more recently, topological insulators [20–23]. An important property of topological insulators is the existence of topologically protected bound states localized on the edge of a sample (see [24] for a recent review), making these systems attractive for applications in quantum technology, and quantum information related fields [25, 26]. For discrete time quantum walks (DTQW) topological phases have been first proposed in one dimension employing a split-step convention by Kitagawa et al. [27, 28]. Since then, further progress has been achieved in the theoretical understanding of topological features of DTQW in the works of Asbóth [29–31]. In particular in Ref. [30] it has been shown that the topological phases of a DTQW can be characterized by a pair of topological invariants (Q_0, Q_π), the possible values of each Q being determined by the symmetry class of the particular system. The numerical value of the topological invariant or topological charge is intimately related to the number of edge states supported, allowing the adoption of an operational meaning to the topological invariants via a scattering formula [32]. This feature of the DTQW is shared with periodically driven quantum systems, including that it may support edge states at two quasi-energies, 0 and π [31, 33]. Realizing topologically protected edge states in quantum walk based synthetic quantum systems is the first step towards applications

in quantum technology. While the localisation has been observed experimentally [20], the full verification of their topological nature, while crucial for applications, has not yet been achieved.

In this Letter we present localized edge states in a DTQW setup and verify their topological origin by directly measuring the respective invariants which forms the basis for a comprehensive exploration of their stability properties. We use a scattering arrangement, as proposed in [30], to determine the topological phases of the corresponding bulk systems. By precisely controlling the disorder in the system we experimentally demonstrate the correspondence between the topological invariants from the scattering setup and the existence of localised edge states on the boundary of two samples. The employed topological invariants fit to the type of disorder realized in the experiment and thus differ from the definition of Ref. [34].

Theoretical Background.— In analogy to its classical counterpart – the random walk – the dynamics of the original DTQW is given by the alternating application of a coin toss \hat{C} and a conditional shift \hat{S} . In the quantum case, the walker can be in a superposition state of positions x and coin states c given by $|\Psi\rangle_t = \sum_x \sum_c a_{x,c}(t) |x\rangle \otimes |c\rangle$ with the time-dependent amplitudes $a_{x,c}(t) \in \mathbb{C}$. Then, the dynamics can be described as $|\Psi\rangle_{t+1} = \hat{U}|\Psi\rangle_t = \hat{S}\hat{C}|\Psi\rangle_t$, with $\hat{C} = \mathbb{1} \otimes \hat{R}(\theta) = \mathbb{1} \otimes e^{-i\hat{\sigma}_x\theta}$ being Pauli rotations in the coin space expressed in the horizontal and vertical basis states $|H\rangle = (1\ 0)^T$ and $|V\rangle = (0\ 1)^T$ and the shift operator $\hat{S} = \hat{T} \otimes |H\rangle\langle H| + \hat{T}^\dagger \otimes |V\rangle\langle V|$ using $\hat{T} = \sum_x |x+1\rangle\langle x|$ and $\hat{T}^\dagger = \sum_x |x-1\rangle\langle x|$. To inves-

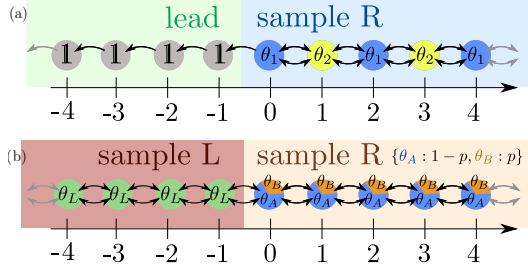


FIG. 1. a) Lead-sample scattering system with alternating coins $\hat{C}_1 = \mathbb{1} \otimes \hat{R}(\theta_1)$ and $\hat{C}_2 = \mathbb{1} \otimes \hat{R}(\theta_2)$. b) Interface between two samples with $\hat{C}_1 = \mathbb{1}$. In the case of the left sample $\hat{C}_2 = \mathbb{1} \otimes \hat{C}_L$, while in the right sample \hat{C}_2 at each site is chosen from θ_A or θ_B , with respective probabilities $1 - p$ and p , yielding disordered systems for $p \neq 0, 1$. The left sample can serve as the lead for scattering experiments, if $\hat{R}(\theta_L) = \mathbb{1}$ is set.

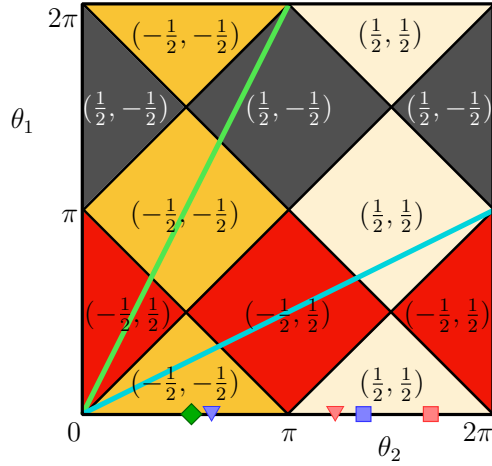


FIG. 2. Topological phase diagram indicating the bulk topological invariants (Q_0, Q_π) as functions of the coin angles θ_1 and θ_2 of a split-step quantum walk. The colored lines and symbols indicate the parameters of the experimentally realised systems.

to investigate topological effects we adopt the split-step protocol, and construct the unitary operator of a single time step as

$$\hat{U} = \hat{S}_- \hat{C}_2 \hat{S}_+ \hat{C}_1, \quad (1)$$

with two coin operators $\hat{C}_{1,2}$, and the asymmetric shift operators $\hat{S}_+ = \hat{T} \otimes |H\rangle\langle H| + \mathbb{1} \otimes |V\rangle\langle V|$ and $\hat{S}_- = \mathbb{1} \otimes |H\rangle\langle H| + \hat{T}^\dagger \otimes |V\rangle\langle V|$. Note, that the split-step scheme is equivalent to two time steps of the original DTWQ given by $\hat{U} = \hat{S} \hat{C}_2 \hat{S} \hat{C}_1$ when alternating two coin operations and relabelling the positions [27, 35]. We will make use of this equivalence for the experimental realisation of the protocol.

For directly measuring the topological invariants we follow the scheme proposed in [30] and study a scattering arrangement comprising a half-infinite lead with

trivial dynamics, e.g. $\hat{U}_{\text{lead}} = \hat{S}_+ \hat{S}_-$ to the left, and a half-infinite sample (a generic split-step quantum walk) to the right, see Fig. 1a. This is the sample of which the topological invariant is to be determined. The generic split-step walk is characterised by the position dependent coin operator $\hat{C}(x) = \sum_x |x\rangle\langle x| \otimes \hat{R}(\theta_x)$ with the formal vector $\theta = (\dots, \theta_0, \theta_1, \dots)$ describing the spatial distribution of the coin angle. For such configurations, Tarasinski et al. [30] derived the scattering formula which relates the pair of bulk topological invariants of the sample to the quasi-energy dependent reflection matrix elements $r(\varepsilon)$ by $(Q_0, Q_\pi) = \frac{1}{2}(r(0), r(\pi))$. The corresponding phase diagram which relates the topological invariants to the two parameters θ_1 and θ_2 characterising the sample is presented in Fig. 2. In an experiment where only a finite number of steps t is implemented, the reflection matrix elements can be approximated by the finite sum

$$r(\varepsilon) \approx \sum_{j=1}^t e^{ij\varepsilon} r_j, \quad (2)$$

which simplifies to a sum or alternating sum for $\varepsilon = 0, \pi$, respectively. The reflected amplitudes r_j are given by the projection of the wave function of an initially localized walker at $x = 0$ in the coin state $|H\rangle$ after j -times application of \hat{U} onto the outgoing state at $x = -1$,

$$r_j = \langle -1, V | \hat{U}^j | 0, H \rangle, \quad (3)$$

following the convention depicted on Fig. 1a. This simple correspondence between reflection amplitudes r_j and the reflection matrix elements $r(\varepsilon)$, allows us to determine the full amplitude information and by this the topological invariants (Q_0, Q_π) in a photonic implementation [35].

When interfacing two semi-infinite samples characterised by different topological invariants exponentially localised states emerge at the edge [27]. Such states are intrinsically robust against perturbations of the sample as long as the topological invariants are preserved. The strength of this topological protection can be probed when exchanging coins in one of the samples and varying its angle and probability, see Fig. 1b).

Experimental Realization.— We implement a photonic quantum walk applying a fibre loop architecture based on the time-multiplexing technique [35] providing great resource efficiency, high homogeneity and long-lasting stability against uncontrolled dephasing [15, 17]. A weak coherent laser pulse plays the role of the walker and its polarization represents the coin state. In combination with standard static linear elements, fast electro-optic modulators (EOM) can be used to switch each pulse individually [14, 17], providing the basis for realising position dependent coin operations. The step operation \hat{S} (or \hat{S}_\pm [36]) is performed by routing the two polarisation components through fibres of different lengths to introduce a well-defined time delay between them. Consequently,

each position in each roundtrip is uniquely represented by discrete time bins, i.e. the position information is mapped into the time domain. Coupling out a small portion of the light in each step and measuring it by a pair of avalanche photo diodes (APD) allows us to observe the polarization resolved time evolution of the walker.

The transformation realised by the EOM, up to a constant phase factor, corresponds to a Pauli x rotation

$$\hat{R}_x(\Phi) = e^{-i\hat{\sigma}_x\Phi} = \begin{pmatrix} \cos \Phi & -i \sin \Phi \\ -i \sin \Phi & \cos \Phi \end{pmatrix}, \quad (4)$$

in the H-V basis [37]. The rotation angle Φ is controlled by applying a voltage U . With a reference voltage U_0 preset for each experiment, the EOM can be dynamically switched between three voltages, $U = 0, \pm U_0$, corresponding to rotation angles $\Phi_U = 0, \pm \Phi_{U_0}$. A Soleil-Babinet Compensator (SBC) placed in front of the EOM is the static realisation of the same transformation (4) at an angle Φ_{SBC} independent from the EOM, yielding three dynamically selectable coin operators,

$$\begin{aligned} \hat{C}_{U=0} &\equiv \hat{R}_x(0)\hat{R}_x(\Phi_{\text{SBC}}) = \hat{R}_x(\Phi_{\text{SBC}}), \\ \hat{C}_{U=\pm U_0} &\equiv \hat{R}_x(\pm \Phi_U)\hat{R}_x(\Phi_{\text{SBC}}) = \hat{R}_x(\Phi_{\text{SBC}} \pm \Phi_U), \end{aligned} \quad (5)$$

with two continuous control parameters Φ_U and Φ_{SBC} . A particular coin distribution θ can be achieved by appropriately programming the switching times of the EOM to address the corresponding pulses, indispensable for the realization of the experimental scenarios depicted on Fig. 1.

Results.— First, we experimentally analyse the topological invariants for samples without disorder in the arrangement shown on Fig. 1a. The scenario requires the experimental implementation of three coin operators, one of which must be the identity, $\mathbb{1}$. Thus, for every preset voltage U_0 the SBC angle is matched to the EOM angle such that $\Phi_{\text{SBC}} = \Phi_{U_0}$, ensuring that the negative voltage $-U_0$ yields the Pauli rotation angle $\Phi_{\text{SBC}} - \Phi_{U_0} = 0$. Consequently, the coin angles of the samples which we can study experimentally must obey $\theta_1 = 2\theta_2$ with $\theta_2 = \Phi_{U_0}$ (green line on Fig. 2), or $\theta_2 = 2\theta_1$ with $\theta_1 = \Phi_{U_0}$ (turquoise line). Scanning along each of these two lines is possible by adjusting the voltage U_0 .

We measure the intensity amplitudes after roundtrip 9 and extract the relative signs of the reflection amplitudes in roundtrip 10 [35], corresponding to performing 5 steps of the split-step walk. The reflection amplitudes r_j are thus reconstructed up to a global sign, allowing us to determine according to Eq. (2) the approximate absolute value and relative sign of the topological invariants Q_0 and Q_π , which is sufficient to identify all topological phase transitions along the green and turquoise lines of Fig. 2. The measurement results for the green line are shown on Fig. 3, along with the simulations for 5 steps, and the expected theoretical values of the bulk topological invariants (the global phases of the measured Q_0 and

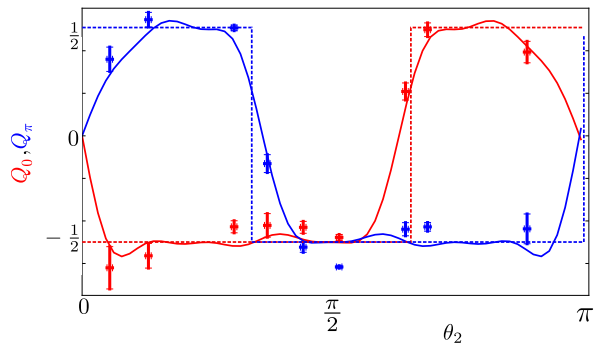


FIG. 3. Pair of topological invariants (Q_0, Q_π) (red and blue colours, respectively) witnessing topological phase transitions, determined using the scheme on Fig. 1a with coin angles θ_1 and θ_2 scanned along green line of Fig. 2. The experimental and simulation results for 5 steps of the split-step walk are shown with circles and solid lines, respectively. The expected theoretical bulk topological invariants are marked with dashed lines. Error bars are obtained by a Monte Carlo simulation [35]

Q_π are chosen to allow for easy comparison). The positions of the observed phase transitions agree well with the theory, and the simulations show that the deviation is dominantly due to finite size effects. The errorbars are obtained via a Monte-Carlo simulation taking the experimental error sources like losses and angle misalignment of the EOM crystal and the SBC into account [35]. In an experimental scan along the turquoise line in Fig. 2 the phase transitions were observed similarly accurately [35].

One of the main features of topological properties is their intrinsic robustness against perturbations, with brings us to our second set of experiments. To test this property we realize disordered samples experimentally, relying on the fast switching capability and easy reprogrammability of the EOM. The considered samples all have $\hat{C}_1 = \mathbb{1}$, while \hat{C}_2 is spatially varied according to Fig. 1b. As a practical simplification the identity operations $\hat{C}_1 = \mathbb{1}$ (both on the lead and the sample side) are taken into account implicitly, allowing us to realize 11 steps of the split-step walk in 11 round trips (see also Fig. 1b). The third available coin operation is still at hand and thus used to introduce disorder as follows. For each θ_x (in the sample) we randomly choose from $\theta_A = \theta$ and $\theta_B = 2\theta$ with the respective probabilities $1 - p$ and p . Therefore, $p = 0.5$ corresponds to maximum disorder, while $p = 0$ to the samples $\hat{C}_2 = \mathbb{1} \otimes \hat{R}(\theta_A)$ and $p = 1$ to $\hat{C}_2 = \mathbb{1} \otimes \hat{R}(\theta_B)$ without any disorder. For this lead-sample system the formula Eq. (2) yields identical results for $r(0)$ and $r(\pi)$ independent of the coin distribution in the sample, and therefore we will consider only $r(0)$ in the following.

In Fig. 4 we present results from two case studies of disordered systems: For each value of p (except the unperturbed systems with $p = 0$ and $p = 1$) we measured

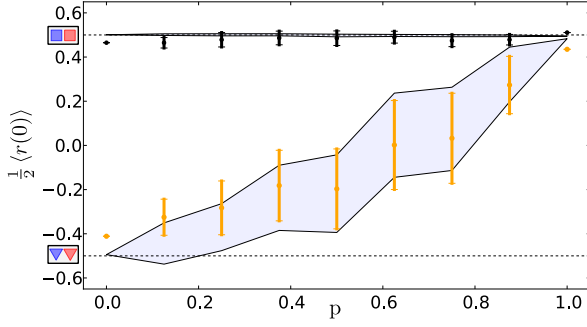


FIG. 4. The (scaled) average reflection matrix element $\frac{1}{2} \langle r(0) \rangle$ for disordered samples; to be compared to the respective bulk topological invariants, $Q_0 = \pm \frac{1}{2}$ (indicated by dashed lines). Black symbols: first case study, represented by squares in Fig. 2 at $\theta_A = 1.68\pi$ and $\theta_B = 1.36\pi$. Orange symbols: second case study, represented by triangles in Fig. 2 at $\theta_A = 0.63\pi$ and $\theta_B = 1.26\pi$. The grey shadings indicate the range of the standard deviations of the simulated values. Error bars are given by the standard deviation of the 50 different ensembles for each noise probability p .

50 randomly generated coin distributions and determined the ensemble average reflection matrix $\langle r(0) \rangle$ after 11 steps, which we compare to the topological invariant Q_0 . Here, we created a reference signal prior to the first step to extract the global phases of the reflection amplitudes [35].

In the first case study (black symbols in Fig. 4) we included coins with $\theta_A = 1.68\pi$ (red square in Fig. 2) and $\theta_B = 1.36\pi$ (blue square), both of which belong to the same topological phase with bulk topological invariants $(Q_0, Q_\pi) = (\frac{1}{2}, \frac{1}{2})$. As expected, the observed value $r(0) \approx \frac{1}{2}$ is approximately independent of the disorder parameter p , confirming that all disordered systems belong to the same topological phase $Q_0 = \frac{1}{2}$. The statistical fluctuations of the 50 ensembles are very small and caused by finite size effects and inevitable experimental inaccuracies.

The second case study (orange symbols in Fig. 4) used coins with $\theta_A = 0.63\pi$ and $\theta_B = 1.26\pi$ (resp. red and blue triangles on Fig. 2), belonging to different topological phases $(-\frac{1}{2}, -\frac{1}{2})$ and $(\frac{1}{2}, \frac{1}{2})$, respectively. We clearly observe a continuous transition from $Q_0 \approx -\frac{1}{2}$ to $Q_0 \approx \frac{1}{2}$ as p is increased from 0 to 1. The high statistical fluctuations indicate that there is no well-defined value of the reflection matrix $r(0)$ in case of disorder ($p \neq 0, 1$), witnessing the lack of a topological invariant in these samples. Detailed analysis of the experimental and numerical data shows that reflection matrix for the individual coin distribution assume either 1 or -1 , and the average value over all 50 configurations is determined by the number of configurations with $r(0) \approx 1$ and $r(0) \approx -1$.

In our last series of experiments, we investigate exponentially localized topologically protected edge states occurring on the boundary of two samples. In the exper-

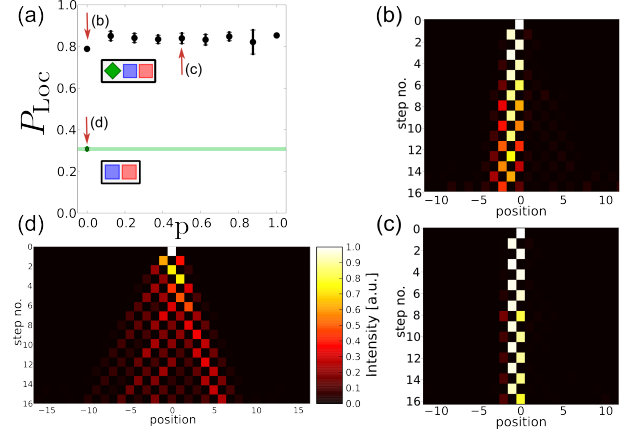


FIG. 5. (a) Black symbols: Localisation as a probability of finding the walker in the central bins versus disorder strength p for the bulk interface with $\theta_A = 1.68\pi$, $\theta_B = 1.36\pi$ and $\theta_L = 0.52\pi$ according to Fig. 1b). Error bars are given by the standard deviation of the 50 different ensembles for each noise probability p . Green symbol: reference system ($\theta_A = 1.36\pi$ and $\theta_L = 1.68\pi$) without localisation extended by a green shaded area indicating the reference value including systematic errors obtained by a Monte-Carlo simulation [35] to allow for comparison. Panels (b), (c), (d) show three wavefunctions for the configurations indicated by the arrows (bright colours denote high, and dark colours low intensities).

imental scenario, depicted on Fig. 1b), a homogeneous sample is implemented on the left, while the right sample is disordered. The samples on the right are identical to those which have been studied in the first case study above, i.e. the coin distribution consisting of the angles $\theta_A = \theta = 1.68\pi$ and $\theta_B = 2\theta = 1.36\pi$ chosen randomly. The control parameter p allows us to tune the extent of disorder, and study the robustness of the edge states against it. The left sample comprises only one coin angle $\theta_L = 3/2 \theta = 0.52\pi$ (squares in Fig. 2)). In a separate scattering experiment we have obtained the value of $\frac{1}{2} \langle r(0) \rangle = -0.581 \pm 0.03$ for the average scaled reflection matrix, revealing the topological invariant $Q_0 = -\frac{1}{2}$ (up to systematic errors [35]). Consequently, this system comprises the interface of two topologically distinct samples, independent of the disorder parameter p , therefore supporting topologically protected edge states on the boundary.

We quantify the degree of localisation by $P_{\text{Loc}} = \sum_{i=-3}^3 P_i$, the probability of finding the walker in the central positions within the interval $[-3, 3]$. After 13 steps, we compare the degree of localization to a reference system exhibiting no localization, consisting of two samples in the same topological phase with respective angles $\theta_L = 1.68\pi$ and $\theta_R = 1.36\pi$ (red and blue squares in Fig. 2). The experimental results for the degree of localization are presented on Fig. 5a. We clearly see that the localisation strength P_{Loc} involving the disordered system (black symbols) is almost three times higher than

for the reference system (green symbol), even when systematic errors via a Monte-Carlo simulation are included (green shaded area). The localisation strength remains roughly constant while increasing the disorder, a clear signature of topological protection of the state. The statistical fluctuations of the 50 configurations per probability p (black error bars) are small compared to the mean values, proving that each single configuration contains a localised bound state.

The panels (b),(c),(d) of Fig. 5 show the three selected wavefunctions in an intensity plot. The presented data sets are concatenated from a low power measurement for the first 6 steps and a high power measurement for the higher steps to avoid detector saturation effects. The two wavefunctions for the localised system exhibit the expected peak of intensities at the positions around at boundary between the two samples, and although belong to the two extremal disorder cases $p = 0$ and $p = 0.5$, their shapes do not differ significantly. On the other hand the wavefunction of the non-localised reference system features the usual double-lobe distribution, each lobe ballistically travelling at the speed determined by the supporting sample.

Conclusion.— Using the time-multiplexing DTQW setup we experimentally studied features of topological insulators, in particular we focussed on localized edge states. A detailed experimental study consisting of direct measurements of the topological invariants enabled us to confirm the robustness and verify the topological origin of the localisation. Due to easy reconfigurability and programmability of the setup we are able to precisely control and tune the disorder strength in ensemble averages over several hundred configurations. The full dynamic control of the system parameters provides a profound basis for the realisation of complex dynamics and can in the future be extended to a second spatial dimension, allowing for more advanced boundary structures and configurations.

This work has received funding from the European Union's Horizon 2020 research and innovation programme under the QUCHIP project GA no. 641039. S.B., T.N., F.E., L.L. and C.S. acknowledge funding by the DFG (Deutsche Forschungsgemeinschaft) via the Gottfried Wilhelm Leibniz-Preis. I. J. have been partially supported by the Czech Science foundation (GAČR) project number 16-09824S, A. G., and I. J. from No. GAČR 13-33906S, RVO 68407700, and A. G. from TÁMOP-4.2.4.A/2-11/1-2012-0001 "National Excellence Program" of Hungary.

[1] Y. Aharonov, L. Davidovich, and N. Zagury, *Physical Review A* **48**, 1687 (1993).
 [2] D. A. Meyer, *Physics Letters A* **223**, 337 (1996).
 [3] E. Farhi and S. Gutmann, *Physical Review A* **58**, 915 (1998).

[4] A. M. Childs, E. Farhi, and S. Gutmann, *Quantum Information Processing* **1**, 35 (2002).
 [5] N. Shenvi, J. Kempe, and K. B. Whaley, *Physical Review A* **67**, 052307 (2003).
 [6] A. Ambainis, J. Kempe, and A. Rivosh, in *Proceedings of the Sixteenth Annual ACM-SIAM Symposium on Discrete Algorithms*, SODA '05 (Society for Industrial and Applied Mathematics, Philadelphia, PA, USA, 2005) pp. 1099–1108.
 [7] A. Ambainis, *SIAM J. Comput.* **37**, 210 (2007).
 [8] A. M. Childs, D. Gosset, and Z. Webb, *Science* **339**, 791 (2013).
 [9] F. W. Strauch, *Physical Review A* **73**, 054302 (2006).
 [10] D. Witthaut, *Physical Review A* **82**, 033602 (2010).
 [11] G. Engel, T. Calhoun, E. Read, T.-K. Ahn, T. Mančal, Y.-C. Cheng, R. Blankenship, and G. Fleming, *Nature* **446**, 782 (2007).
 [12] M. Mohseni, P. Rebentrost, S. Lloyd, and A. Aspuru-Guzik, *The Journal of Chemical Physics* **129**, 174106 (2008).
 [13] C.-W. Lee, P. Kurzyński, and H. Nha, *Physical Review A* **92**, 052336 (2015).
 [14] A. Schreiber, K. N. Cassemiro, V. Potoček, A. Gábris, I. Jex, and C. Silberhorn, *Physical Review Letters* **106**, 180403 (2011).
 [15] A. Schreiber, K. N. Cassemiro, V. Potoček, A. Gábris, P. J. Mosley, E. Andersson, I. Jex, and C. Silberhorn, *Physical Review Letters* **104**, 050502 (2010).
 [16] A. Crespi, R. Osellame, R. Ramponi, V. Giovannetti, R. Fazio, L. Sansoni, F. De Nicola, F. Sciarrino, and P. Mataloni, *Nat Photon* **7**, 322 (2013).
 [17] F. Elster, S. Barkhofen, T. Nitsche, J. Novotný, A. Gábris, I. Jex, and C. Silberhorn, *Scientific Reports* **5**, 13495 (2015).
 [18] A. Schreiber, A. Gábris, P. P. Rohde, K. Laiho, M. Štefaňák, V. Potoček, C. Hamilton, I. Jex, and C. Silberhorn, *Science* **336**, 55 (2012).
 [19] P. M. Preiss, R. Ma, M. E. Tai, A. Lukin, M. Rispoli, P. Zupancic, Y. Lahini, R. Islam, and M. Greiner, *Science* **347**, 1229 (2015).
 [20] T. Kitagawa, M. A. Broome, A. Fedrizzi, M. S. Rudner, E. Berg, I. Kassal, A. Aspuru-Guzik, E. Demler, and A. G. White, *Nature Communications* **3**, 882 (2012).
 [21] C. Poli, M. Bellec, U. Kuhl, F. Mortessagne, and H. Schomerus, *Nature Communications* **6**, 6710 (2015).
 [22] J. M. Zeuner, M. C. Rechtsman, Y. Plotnik, Y. Lumer, S. Nolte, M. S. Rudner, M. Segev, and A. Szameit, *Physical Review Letters* **115**, 040402 (2015).
 [23] F. Cardano, M. Maffei, F. Massa, B. Piccirillo, C. de Lisi, G. De Filippis, V. Cataudella, E. Santamato, and L. Marrucci, *arXiv:1507.01785* (2015).
 [24] M. Z. Hasan and C. L. Kane, *Rev. Mod. Phys.* **82**, 3045 (2010).
 [25] D. Hsieh, Y. Xia, D. Qian, L. Wray, J. H. Dil, F. Meier, J. Osterwalder, L. Patthey, J. G. Checkelsky, N. P. Ong, A. V. Fedorov, H. Lin, A. Bansil, D. Grauer, Y. S. Hor, R. J. Cava, and M. Z. Hasan, *Nature* **460**, 1101 (2009).
 [26] S. Moulieras, M. Lewenstein, and G. Puentes, *Journal of Physics B: Atomic, Molecular and Optical Physics* **46**, 104005 (2013).
 [27] T. Kitagawa, M. S. Rudner, E. Berg, and E. Demler, *Physical Review A* **82**, 033429 (2010).
 [28] T. Kitagawa, *Quantum Information Processing* **11**, 1107 (2012).

- [29] J. K. Asbóth, Physical Review B **86**, 195414 (2012).
- [30] B. Tarasinski, J. K. Asbóth, and J. P. Dahlhaus, Physical Review A **89**, 042327 (2014).
- [31] J. K. Asbóth and H. Obuse, Physical Review B **88**, 121406 (2013).
- [32] I. C. Fulga, F. Hassler, A. R. Akhmerov, and C. W. J. Beenakker, Phys. Rev. B **83**, 155429 (2011).
- [33] L. Jiang, T. Kitagawa, J. Alicea, A. R. Akhmerov, D. Pekker, G. Refael, J. I. Cirac, E. Demler, M. D. Lukin, and P. Zoller, Physical Review Letters **106**, 220402 (2011).
- [34] C. Cedzich, F. A. Grünbaum, C. Stahl, L. Velázquez, A. H. Werner, and R. F. Werner, Journal of Physics A: Mathematical and Theoretical **49**, 21LT01 (2016).
- [35] For details see supplementary material.
- [36] In this case the choice of convention is a matter of taste.
- [37] T. Nitsche, F. Elster, J. Novotný, A. Gábris, I. Jex, S. Barkhofen, and C. Silberhorn, arXiv:1601.08204 [quant-ph] (2016), arXiv: 1601.08204.

Supplemental Material: Measuring Topological Invariants and Protected Bound States in Disordered Discrete Time Quantum Walks

SECTION 1: EXPERIMENTAL SETUP

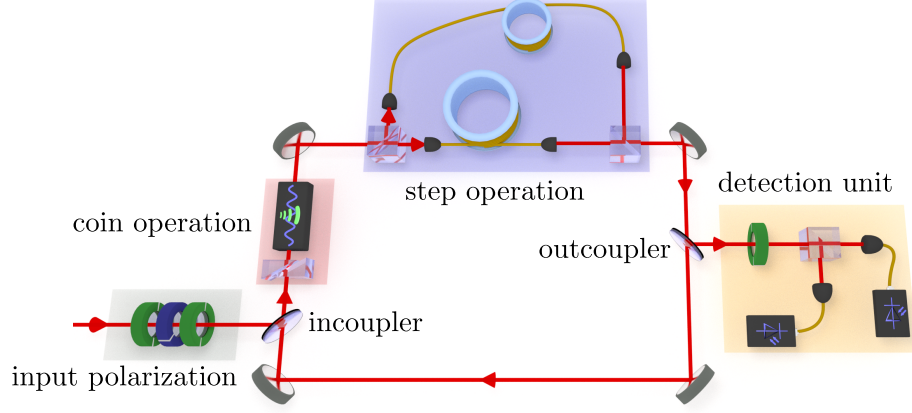


FIG. S1. Setup sketch of the quantum walk, for the description see text.

To implement the discrete time quantum walk (DTQW), we make use of a time-multiplexing loop setup, as it was for the first presented in [S1], see Fig. S1. Here, a Soleil-Babinet compensator (SBC) and electro-optic modulator (EOM) realise the dynamic coin operation (red area) according to the matrices in eqs. (4) and (5) in the main text. Two standard single-mode fibres of different lengths and two polarizing beam splitters (PBS) implement the step operator (blue area). A quarter wave plate in front of the detection unit comprising two avalanche photodiodes and a PBS for polarization resolving measurements (orange area) performs a basis transform for the extraction of relative phases, as described in section 3. The three input waveplates can generate an arbitrarily polarized input state and compensate for polarization rotations of the incoupler (grey area).

SECTION 2: TOPOLOGICAL INVARIANTS FOR A 2. SYSTEM

Just by reprogramming the switching times of the EOM we can change the order of \hat{C}_1 and \hat{C}_2 to measure the topological invariants for a second system (see Fig. S2). This pattern corresponds to scanning along the turquoise line in the parameter plot (Fig. 2, main text). Here the positions of the phase transitions between same sign and opposite sign of Q_0 and Q_π take place at different angles compared to Fig. 3 in the main text. We find the same sign for $\theta_1 = 0.73\pi$, opposite sign for $\theta_1 = 1.12\pi$ and a transition region for $\theta_1 = 0.90\pi$ in accordance with the finite-step simulation.

SECTION 3: SIGN EXTRACTION

In order to extract the topological invariants we need to measure the reflection amplitudes, i.e. the intensities as well as the phases according to eq. (3) in the main text. For the given coin operators (eq. (4), main text) the reflection amplitudes are purely imaginary [S2] therefore only their sign needs to be determined. In the experiment, phase measurements have to be carried out separately as the APDs only give us the intensity information. Therefore, we have included an additional transformation to create interference between pulses belonging to neighbouring positions to determine their relative signs. For example, to obtain full amplitude information for the 3rd step, we use EOM settings equivalent to the beam-splitter cascade on Fig. S3. Note that the figure shows two intensity measurements: the intensities are extracted one roundtrip before the last one, while the sign information is determined in a second measurement carried out in the final roundtrip. The interference between successive reflection amplitudes is realised by switching the EOM to a mixing coin $\hat{R}_x(\alpha)$ instead of the identity in the lead region (blue coins). Again, the choice

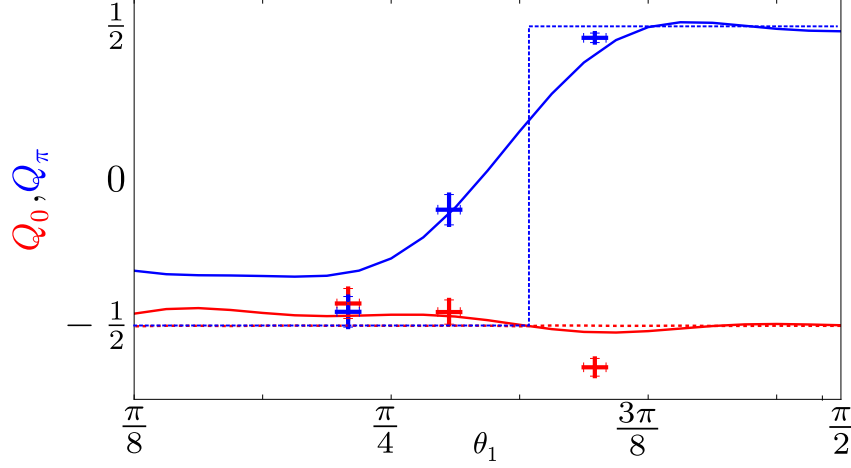


FIG. S2. Topological invariants Q_0 (red symbols) and Q_π (blue symbols), simulations for 5 steps of the split-step walk (solid lines), and theoretical values of the bulk topological invariants (dashed lines) for a scan along the turquoise line in Fig. 2 in the main text. Error bars are obtained by a Monte Carlo simulation (see section for details).

of α is restricted by the EOM capabilities to the angles corresponding to \hat{C}_1 or \hat{C}_2 (yellow and blue diamonds). After two neighbouring pulses interfered in succession of the corresponding coin operation we couple them out (as in every step) and route them to the detection unit. The pulses pass then a tomography QWP at 45° , and are afterwards measured in a polarization resolved way. The relative sign between the two pulses can be extracted from the intensity difference in the H- and V-detectors as shown in the following calculus: The complex wave function at e.g. position $x = -4$ is given by

$$\begin{aligned}
 |\Psi\rangle_{-4} &= \hat{C}_{\text{QWP}} \left[\hat{P}_H \hat{R}_x(\alpha) \begin{pmatrix} 0 \\ r_1 \end{pmatrix} + \hat{P}_V \hat{R}_x(\alpha) \begin{pmatrix} 0 \\ r_2 \end{pmatrix} \right] \\
 &= \frac{1}{\sqrt{2}} \begin{pmatrix} 1 & i \\ i & 1 \end{pmatrix} \left[\hat{P}_H \begin{pmatrix} \cos \alpha & -i \sin \alpha \\ -i \sin \alpha & \cos \alpha \end{pmatrix} \begin{pmatrix} 0 \\ r_1 \end{pmatrix} \right. \\
 &\quad \left. + \hat{P}_V \begin{pmatrix} \cos \alpha & -i \sin \alpha \\ -i \sin \alpha & \cos \alpha \end{pmatrix} \begin{pmatrix} 0 \\ r_2 \end{pmatrix} \right] \\
 &= \frac{1}{\sqrt{2}} \begin{pmatrix} -ir_1 \sin \alpha + ir_2 \cos \alpha \\ r_1 \sin \alpha + r_2 \cos \alpha \end{pmatrix}
 \end{aligned}$$

where $\hat{P}_H = \begin{pmatrix} 1 & 0 \\ 0 & 0 \end{pmatrix}$ and $\hat{P}_V = \begin{pmatrix} 0 & 0 \\ 0 & 1 \end{pmatrix}$ are the projectors on the horizontal and vertical basis element, respectively, and r_j the (vertically polarized) reflection amplitudes. This means that the intensity measured in the H-(V-) detector behind the PBS reads

$$I_{H/V} = \frac{1}{2} (r_1^2 \sin^2 \alpha \mp 2r_1 r_2 \sin \alpha \cos \alpha + r_2^2 \cos^2 \alpha).$$

It follows, that by knowing the intensity difference,

$$\Delta I = I_H - I_V = -2r_1 r_2 \sin(\alpha) \cos(\alpha), \quad (\text{S1})$$

of the two detectors, and the EOM angle α one can determine the relative signs of r_1 and r_2 . In particular for $\alpha \in [0, \pi/4]$, if the intensity in the H-detector is smaller than in the V-detector then r_1 and r_2 have the same sign, while the intensity is larger in the H- than in V-detector we have $\text{sign}(r_1) \neq \text{sign}(r_2)$. In this way we can sequentially determine every sign relation between every successive reflection amplitude r_j and r_{j+1} , enabling us to reconstruct the sign of every amplitude relative to the first one.

In order to determine the global sign of all amplitudes, it is necessary to use a reference pulse. We have created the reference pulse by putting a known wave plate aligned at well-defined angle, realizing the transformation \hat{C}_{ext} (grey diamond), before the input is coupled into the loop. Thus, the reference pulse with known phase from the input state (orange shaded region) is split off in the first roundtrip. At the price of this additional roundtrip we are able to compare the first reflection amplitude r_1 with the reference pulse and by this means obtain the global sign.

Since only sign changes between neighbours can be extracted, the described method is very sensitive to errors: if one sign is extracted the wrong way all following signs will also be wrong. This issue becomes most serious for angles α close to multiples of $\pi/2$, because then the intensity difference Eq. (S1) goes to zero. The same is true if one or both of the amplitudes r_j become very small. For the presented results on the stability properties of the topological invariants in Fig. 4 in the main text, we successfully performed the sign extraction in step 5 (which means after 10 roundtrips) which proves the high accuracy of the experimental setup.

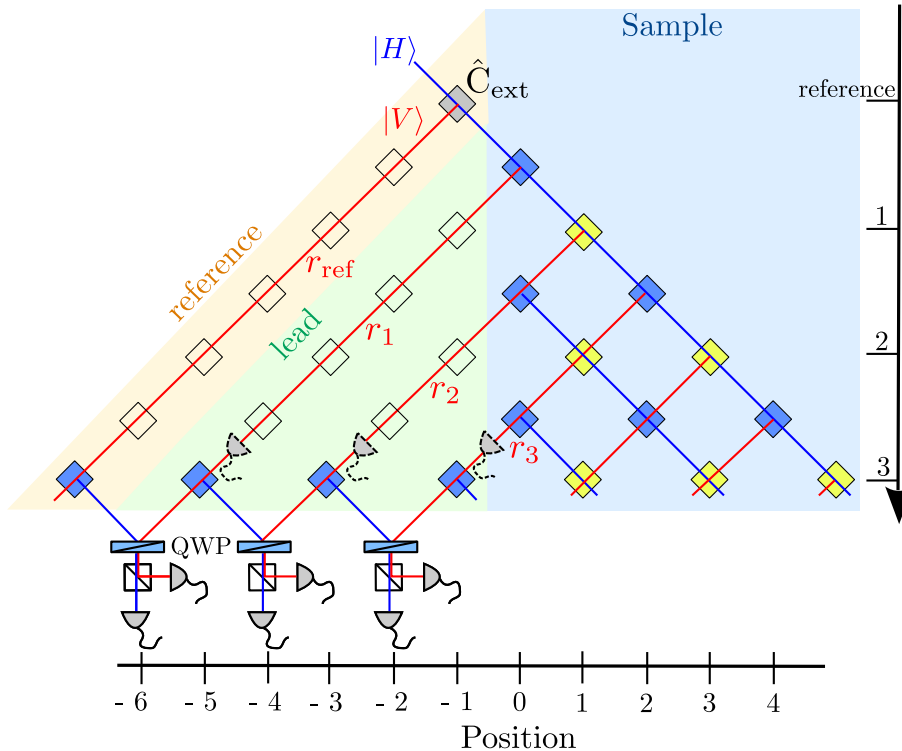


FIG. S3. Scheme of the split step quantum walk with the intensity and phase extraction (here exemplary for the third step). The intensity is measured by the detectors indicated by dashed lines, while the relative signs of neighbored positions are extracted one roundtrip later in a tomographic measurement. Note that in general we couple out a small portion of the light in every roundtrip for detection, but for the actual measurement we analyse only the two indicated steps. The transparent diamonds correspond to the identity coin in the lead region (green shaded) and the blue and yellow diamonds to \hat{C}_1 and \hat{C}_2 respectively (sample, blue shaded). The paths the two polarizations can take are marked in red (vertical) and blue (horizontal). An external coin outside the loop is marked by a grey diamond and used as a reference signal for the phase extraction (orange shaded).

SECTION 4: ERRORBARS

We have identified four sources of systematic errors in our experimental setup, compare also [S3]: first, the detector and power dependent detection efficiencies, which were determined in a separate measurement; second, the different losses experienced in different paths due to dissimilar coupling efficiencies and path geometries, which are estimated in an independent measurement with an accuracy of $\pm 3\%$; third, the exact angle of the (switched) EOM which can only be determined up to $\pm 1^\circ$; fourth, the angle of the SBC can be set only with a precision of 1° .

The power dependence of the detector efficiencies plays only a role in those experiments where the full time evolution of the wave function is tracked (see Fig. 5 in the main text). For these chessboard patterns of the (localised) states we concatenate measurements with two different initial power levels: First, we introduce a neutral-density-filter (ND-filter) with an optical density of 4 in the input beam which allows for reliable detection of the first steps, however, with a very limited maximal observable step number. Thus, we perform a second measurement employing a ND-filter

with an optical density of 1: Here the detectors saturate in the first steps, but we are able to resolve up to 16 steps.

For the determination of the parameters of the other three errors we resorted to a numerical model. In a Monte-Carlo simulation we randomly chose 1000 sets from the parameters within the identified ranges. The set yielding the best reproduction of the experimental data (we calculated the distance between simulation and experiment for the first 7 roundtrips) was chosen for the realistic model. The mean deviation of the statistics produced by the Monte Carlo simulation from the realistic model determines the size of the presented errorbars.

SECTION 5: SPLIT STEP SCHEME

For the investigation of topological effects in DTQW originally a split-step scheme consisting of two coin operations in between the asymmetric step operators \hat{S}_\pm was proposed [S2, S4]. It is fully equivalent to two steps with the symmetric step operator \hat{S} and alternating coins when relabelling the positions in every second step, as demonstrated in Fig. S4.

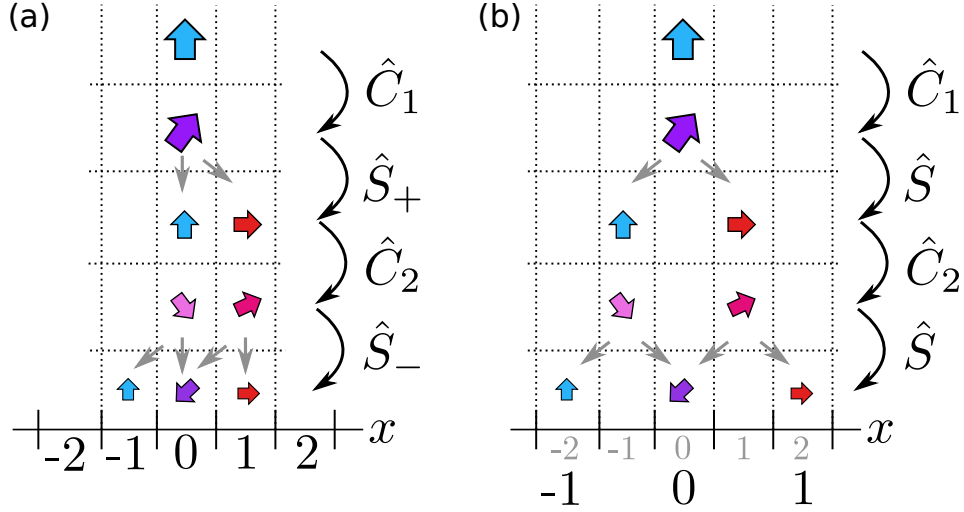


FIG. S4. Exemplary evolution of a quantum walker's wavefunction (coloured arrows) (a) Originally proposed split-step scheme according to $\hat{U} = \hat{S}_- \hat{C}_2 \hat{S}_+ \hat{C}_1$; (b) Experimental realisation of the split step scheme using a double step protocol governed by $\tilde{U} = \hat{S} \hat{C}_2 \hat{S} \hat{C}_1$ with subsequent position relabelling (original labels: grey; after relabelling: black); for simplicity, we chose a vertically polarized input state (blue arrow)

-
- [S1] A. Schreiber, K. N. Cassemiro, V. Potoček, A. Gábris, P. J. Mosley, E. Andersson, I. Jex, and C. Silberhorn, *Physical Review Letters* **104**, 050502 (2010).
 - [S2] B. Tarasinski, J. K. Asbóth, and J. P. Dahlhaus, *Physical Review A* **89**, 042327 (2014).
 - [S3] F. Elster, S. Barkhofen, T. Nitsche, J. Novotný, A. Gábris, I. Jex, and C. Silberhorn, *Scientific Reports* **5**, 13495 (2015).
 - [S4] T. Kitagawa, M. S. Rudner, E. Berg, and E. Demler, *Physical Review A* **82**, 033429 (2010).